THE JOURNAL OF PHYSICAL CHEMISTRY C

ARTICLE

pubs.acs.org/JPCC

Role of Nd^{3+} Ions in Modifying the Band Structure and Photocatalytic Properties of Substituted Indium Titanates, $In_{2(1-x)}Nd_{2x}TiO_5$ Oxides

Mrinal R. Pai,*[,†] Jerina Majeed,[†] Atindra M. Banerjee,[†] Ashok Arya,[‡] Shovit Bhattacharya,[§] Rekha Rao,[∥] and Shyamala R. Bharadwaj[†]

[†]Chemistry Division, [‡]Material Science Division, [§]Technical Physics Division, and [∥]Solid State Physics Division, Bhabha Atomic Research Centre, Mumbai-400085, India

ABSTRACT: We report here the role of Nd^{3+} ions in modifying the band structure of indium titanate and enhancement of photocatalytic evolution of H_2 from H_2O−methanol mixtures in both sunlight and visible irradiation over Nd^{3+}−$In^{3+}{}_2Ti^{4+}O_5$ oxides. A series of neodymium, isovalent to In^{3+} ion, were doped at the A-site in indium titanate ($In_{2(1-x)}Nd_{2x}TiO_5$) samples by means of a solid-state reaction and characterized by different techniques. First-principles local-density band structure calculations were performed here for the first time on Nd-doped In_2TiO_5 to analyze the distribution of valence states of Nd, Ti, In, O atoms near the Fermi level. The photocatalytic activities have been investigated for all of the substituted and unsubstituted samples under sunlight, visible, and UV−visible irradiation. Isovalent doping of neodymium ions was attempted with an objective to suppress the formation of nonstoichiometric defects, which would otherwise work as nonradiative recombination centers between photogenerated electrons and holes. Raman spectra in agreement with FTIR, XRD, and theoretical calculations demonstrated that the neodymium ion has been successfully incorporated into the lattice of In_2TiO_5, accompanied by an increase in cell volume, while a secondary phase of $Nd_2Ti_2O_7$ was segregated beyond 10% Nd substitution. An optimal dosage of 10% Nd^{3+} ion doping, with $In_{1.8}Nd_{0.2}TiO_5$ abbreviated as ITNd(2), resulted in significant enhancement in photocatalytic H_2 yield, while In_2TiO_5 has not shown any visible light photoactivity. The decreasing order of catalytic activity is as follows: ITNd(2) > ITNd(3) > ITNd(1) > ITNd(4) > In_2TiO_5, The effect of different experimental conditions, duration of irradiation, and the presence of cocatalyst on the yield of hydrogen was also monitored. Maximum apparent quantum efficiency (AQE) of ~4.5% was achieved with Pt/ITNd(2). First-principles calculations reveal that Nd is one of the elements that are able to make a valence-band position higher than O 2p orbitals, thereby resulting in a narrowing of the band gap by 0.82 eV. We propose that the introduction of the Nd plays a crucial role in visible light photosensitization and enhancement of the electron−hole separation.

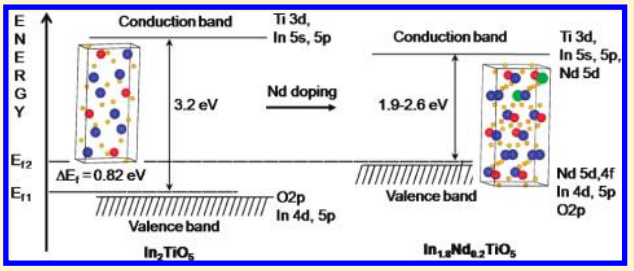

1. INTRODUCTION

Efficient photocatalytic hydrogen generation from water is attractive as it provides a viable solution for energy- and environment-based issues that arised due to depleting fossil fuels and evolution of green house gases. In the search for efficient photocatalysts under visible light for direct splitting of water, a variety of semiconductors based on TiO_2, metal oxides, nitrides, sulphides, oxysulfides, oxynitrides, niobates, tantalates, and titanates have been extensively studied and have been reviewed in several articles.[1−4] Representative photocatalysts reported so far include $SrTiO_3$,[5−7] $Na_2Ti_6O_{13}$,[8] $BaTi_4O_9$,[9] $K_4Nb_6O_{17}$,[10,11] $K_2Ti_4O_9$,[12] $K_2La_2Ti_3O_{10}$,[5,13] $K_3Ta_3Si_2O_{13}$,[14] $K_2Sr_{1.5}Ta_3O_{10}$,[15] $LiCa_2Ta_3O_{10}$,[16] $BaCeO_3$,[17] CeO_2:Sr,[18] Ga_2O_3:Zn,[19] and $AgLi_{1/3}Ti_{2/3}O_2$,[20] which show potential activities for the decomposition of pure water. Attempts have also been made to develop newer visible-light photocatalysts, such as $Cd_{1-x}Zn_xS$ ($0.2 < x < 0.35$),[21] $(CuAgIn)_xZn_{2(1-x)}S_2$,[22] $Na_{14}In_{17}Cu_3S_{35}$,[23] Fe_2O_3, and WO_3.[24] Perovskite-type oxides[25−30] have recently attracted much attention because of their high photocatalytic activities under UV irradiation and, more remarkably, under visible light. Cr- or Fe-doped $La_2Ti_2O_7$[31,32] was reported to show visible-light-induced activity toward isopropyl alcohol degradation to CO_2. The undoped single Aurivillius phase oxides, $PbBi_2Nb_2O_9$,[33] Bi_2WO_6,[34] and Bi_2MoO_6,[35] are active for an O_2 evolution reaction under visible light irradiation but are inactive for H_2 evolution due to the low conduction band level. The target set for efficient water splitting into H_2 and O_2 is 30% in terms of a quantum yield at 600 nm equivalent to ~5% of solar energy conversion. The $Cr_xRh_{2-x}O_3$/GaN:ZnO[36] and $Ru/SrTiO_3$:Rh-$BiVO_4$[37] photocatalysts respond to about 500 nm for overall water splitting, approaching this target, but the quantum yield is still low.[4] However, this research area is progressing, and reports have proven that highly efficient water splitting is actually possible using powdered photocatalysts. Yet still the development of new and superior photocatalyst materials is a major issue.

Substantial progress has been made to extend the wavelength range of UV-active oxides into the visible range by the substitutional doping of metals as in $In_{1-x}Ni_xTaO_4$[38] and (V-, Fe-, or Mn-)

Received: August 17, 2011
Revised: November 11, 2011
Published: December 08, 2011

Table 1. Abbreviations, Lattice Parameters, and Phase Identification by XRD of $In_{2(1-x)}Nd_{2x}TiO_5$ Samples

sample no.	nominal composition	2x	abbreviation ITNd(2x)	phase identified by XRD, supported by FTIR and Raman spectra	a (Å)[a]	b (Å)	c (Å)	vol (Å^3)
1	In_2TiO_5	0.0	ITNd(0)	In_2TiO_5	*7.24203*	*3.50044*	*14.89654*	*377.631*
					(0.00172)	*(0.00076)*	*(0.00477)*	*(0.175)*
					7.246	3.433	14.881	370.172 (Figure 3a)
2	$In_{1.9}Nd_{0.1}TiO_5$	0.1	ITNd(1)	In_2TiO_5	*7.24504*	*3.51294*	*14.89807*	*379.176*
					(0.00238)	*(0.00205)*	*(0.00515)*	*(0.287)*
3	$In_{1.8}Nd_{0.2}TiO_5$	0.2	ITNd(2)	In_2TiO_5	*7.24357*	*3.51218*	*14.89572*	*378.957*
					(0.00248)	*(0.00217)*	*(0.00534)*	*(0.304)*
					7.259	6.866	14.881	741.709 (SC1, Figure 3b)
4	$In_{1.7}Nd_{0.3}TiO_5$	0.3	ITNd(3)	major In_2TiO_5 and minor $Nd_2Ti_2O_7$	*7.26391*	*3.51302*	*15.02808*	*383.490*
					(0.00782)	*(0.00772)*	*(0.01879)*	*(1.051)*
5	$In_{1.6}Nd_{0.4}TiO_5$	0.4	ITNd(4)	major In_2TiO_5 and minor $Nd_2Ti_2O_7$	*7.25219*	*3.50576*	*14.91879*	*379.302*
					(0.00567)	*(0.00272)*	*(0.00925)*	*(0.479)*
					7.266	6.866	14.881	742.392 (SC2, Figure 3c)

[a] Lattice parameters obtained by Indexing Powderex Prog[46] in italic. Lattice parameters obtained by first principles in roman.

TiO_2[39] or by the doping of C, N, and S as in $TiO_{2-x}N_x$,[40] $TiO_{2-x}C_x$,[41] TaON,[42] and $Sm_2Ti_2O_5S_2$.[43] Dopants such as N, Fe, and Cr induced the visible light absorption, but, simultaneously, substitution-induced defects were created, which serve as sites for electron−hole recombination that leads to low quantum yields. The In_2TiO_5 is composed of the octahedral $[TiO_6]$ and $[InO_6]$ motifs, containing both early transition metal (d_0) and p-block metal (d_{10}) that fulfills desirable criterion required for active photocatalyst. Up to now, very few studies are reported on the In_2TiO_5 as a potential photocatalyst.[44,45] Recently, we have shown enhanced photocatalytic activity of In_2TiO_5 nanoparticles as compared to commercial TiO_2 (P25) and bulk photocatalyst;[45] also crystallinity and surface area of indium titanate nanoparticles were optimized to achieve maximum H_2 yield. Here, with an objective to extend the photoresponse and to enhance the photocatalytic activity of UV-active In_2TiO_5 oxides in the visible photoillumination, substitution of Nd^{3+} ions at A-site in In_2TiO_5 was attempted. In this Article, varying amounts of isovalent substitution by Nd^{3+} cations at In^{3+} site were preferred, to prevent the formation of nonstoichiometric oxygen defects (δ) that otherwise would act as recombination centers for photogenerated holes and electrons. Thus, we expect that In_2TiO_5, the only ternary compound of the In/Ti/O system, and its modified form after Nd^{3+} substitution may also result in excellent photoactivity for the said reaction.

A series of $In_{2(1-x)}Nd_{2x}TiO_5$ photocatalysts were synthesized via the solid-state route and characterized by X-ray diffraction (XRD), Raman, infrared (FTIR), N_2-BET sorption, scanning electron microscopy (SEM), and photoluminescence (PL) spectra. The influence of metal ion substitution on band gap was measured by UV−visible diffusive reflective spectroscopy (DRS). First-principles local density approximation (LDA)-based tight-binding linear muffin-tin orbital (TB-LMTO) calculations were performed to understand the role played by Nd dopant ions in modifying the electronic structure of In_2TiO_5 and in enhancing their photoresponse, in sunlight/visible light. Here, we describe photocatalytic H_2 generation using $In_{2(1-x)}Nd_{2x}TiO_5$ under sunlight, visible, and UV−visible irradiation observed for long durations. Also, the effect of various experimental conditions on photo activity was evaluated: different environments inside the reaction cell (evacuation, argon purging), duration of irradiation, and presence/absence of cocatalyst. Apparent quantum efficiencies obtained as a function of Nd substitution irradiated under visible, sunlight, and UV−visible light sources were calculated.

2. EXPERIMENTAL AND THEORETICAL METHODS

2.1. Synthesis of Catalyst/Co-catalyst. Mixed oxides with nominal composition $In_{2(1-x)}Nd_{2x}TiO_5$ were synthesized through the ceramic route by mixing reactant oxides in appropriate stoichiometry as depicted by the following equations: $(1-x)In_2O_3 + TiO_2 + xNd_2O_3 \rightarrow In_{2(1-x)}Nd_{2x}TiO_5$ ($2x = 0.0$, 0.1, 0.2, 0.3, and 0.4) abbreviated as mentioned in Table 1. The pellets of homogeneous mixtures were calcined, first at 650 °C followed by high temperature calcination at 800, 1000, and finally at 1250 °C for 24 h, with intermittent grindings so as to ensure the uniformity and the completion of the reaction.

To further improve the photocatalytic hydrogen production, Pt as cocatalyst (1% by weight) was loaded on the ITNd(2) sample, by the photo deposition method. For this purpose, 0.1 g of the catalyst along with 25 mL of water and 5 mL of ethanol was mixed with 0.2 mL of H_2PtCl_6 purged with Ar gas and then irradiated under UV light for about 2 h. The sample was then washed with ethanol and dried.

2.2. Characterization. *2.2.1. XRD and N_2 BET.* The powder XRD patterns were recorded on a Philips diffractometer (model PW 1710), equipped with a graphite monochromator and Ni-filtered Cu K_α radiation. The patterns were indexed using the Powderx program[46] for determination of the unit cell parameters of the substituted samples. The crystallite size, D, was calculated from the XRD line width according to the Scherrer equation:

$$\Delta(2\theta) = \frac{K\lambda}{\beta(\cos\theta)}$$

where $\Delta(2\theta)$ is the width at half-maximum intensity (in radians) and θ is the Bragg angle of the (203) plane in the diffraction pattern of the peak, K is a constant, depending on the line shape profile (currently $K = 0.9$), λ is the wavelength of the X-ray source (in the case of Cu radiation, $\lambda = 0.154059$ nm), and β is the crystallite size in nanometers.[47] A Quantachrome Autosorb-1 analyzer was employed for measurement of N_2-BET surface area by recording the nitrogen adsorption isotherms.

dx.doi.org/10.1021/jp207904k | J. Phys. Chem. C 2012, 116, 1458–1471

2.2.2. FTIR and Raman Spectroscopic Studies. Vibrational spectra of samples were recorded on a Fourier transform infrared spectrophotometer model FTIR-600, JASCO, Japan. FTIR spectra of all of the samples were recorded in the mid-IR region (4000−400 cm^{-1}). Dry KBr (∼200 mg) was mixed with the sample (∼2.5 mg) and ground for homogenization. The mixture was pelletized to a thin wafer like transparent pellet at ∼5 tons cm^{-2}. These pellets were used for IR spectral measurements. Raman spectra were recorded using 532 nm lines from a diode Nd:YAG laser (power 15 mW) focused to a spot size of about 20 μm. The scattered light was analyzed using a home-built 0.9 m single monochromator coupled with a super notch filter and detected by a cooled charge couple device (CCD, Andor Technology). The entrance slit was kept at 50 μm, which gave a resolution limited line width of 3 cm^{-1}.

2.2.3. Photoluminescence Spectra. All luminescence measurements were carried out at room temperature with a resolution of 3 nm, using Edinburgh Instruments' FLSP 920 system having a 450 W Xe lamp as the excitation source. All emission spectra were corrected for the detector response. Finely powdered samples were dispersed on a slide using methanol as dispersing medium. All of the samples were excited at a wavelength of 230 nm.

2.2.4. Scanning Electron Microscope. For microstructural examination under a scanning electron microscope (SEM), a thin layer of gold (100 Å) was coated on the calcined and sintered pellets at 1400 °C by thermal evaporation in a vacuum coating unit. A measured quantity of gold wire (99.99% pure) was wrapped on a tungsten wire, which in turn was heated to evaporate the gold wire. The images of gold-coated samples were recorded on scanning electron microscope model Tescan Vega MV 2300T/40 using an accelerating voltage of 25 kV at the working distance of ∼10 mm.

2.2.5. Diffuse Reflectance Spectroscopy. Band gap measurements of all semiconductor oxide samples were estimated by recording their diffuse reflectance UV−visible spectra using a spectrophotometer of JASCO model V-530, Japan, scanned in the range of 200−1000 nm at the scanning speed of 200 nm/min.

2.3. Catalyst Photoactivity. *2.3.1. Photoactivity under Sunlight.* Photocatalytic activity was evaluated in a rectangular quartz reactor of dimensions (10 × 2.1 × 2.1 cm^3), equipped with a sampling port provided with a septum through which the gas mixture could be removed for analysis. 0.1 g of catalyst was kept in contact with water + methanol mixtures (total volumes of 15 mL, 2:1 v/v %). Normally, in photocatalytic activity experiments, reactions mixtures are purged with argon before irradiation; to provide air free conditions as oxygen acts as e-scavenger, also it gets photoadsorbed on the photocatalysts and blocks the active sites for the reaction. Therefore, here reaction mixtures were either purged with argon or evacuated before irradiation. The water−methanol mixtures suspended with photocatalyst were then irradiated under sunlight for a duration of 6 h during the afternoon (1030 to 1630 h IST). The reaction products were analyzed every 2 h using a gas chromatograph (Netel (Michro-1100), India) equipped with a thermal conductivity detector (TCD); molecular sieve column with argon as carrier was employed in the isothermal temperature mode at 50 °C oven temperature.

2.3.2. Photoactivity under Visible Irradiation. To eliminate the wavelengths in UV region, and to complement the sunlight results, the photoactivity of all samples was also evaluated under white light illumination under conditions similar to those

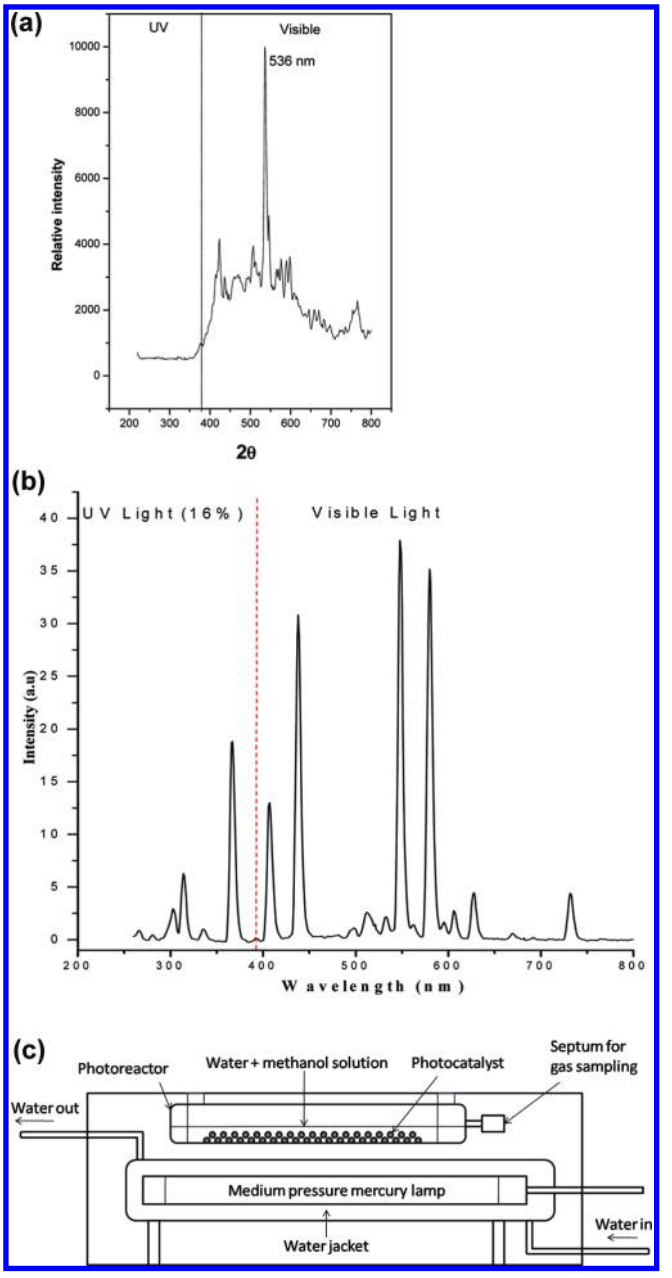

Figure 1. Typical outer irradiation reaction assembly for evaluation of photoactivity of $In_{2(1-x)}Nd_{2x}TiO_5$ samples under UV−visible and visible irradiation. Emission spectra of (a) visible medium pressure mercury lamp (Hg, SAIC, India, 400 W), and (b) UV−visible medium pressure mercury lamp (Hg, Ace Glass Inc., 450 W). (c) The outer irradiation assembly where the photoreactor is placed parallel to the source of light.

explained in section 2.3.1. The samples were irradiated under a water-cooled medium-pressure mercury lamp (Hg, SAIC, India, 400 W), which emits wavelengths longer than 400 nm (λ_{max} = 536 nm) as shown in Figure 1a.

2.3.3. Photoactivity under UV−Visible Irradiation. Because all samples did not show photoresponse in visible light, hence their photoactivity was evaluated and compared under UV−visible light. The samples were irradiated under a medium-pressure mercury lamp (Hg, Ace Glass Inc., 450 W), which emits not only ultraviolet light, but also visible light, and wavelengths in the

dx.doi.org/10.1021/jp207904k | J. Phys. Chem. C 2012, 116, 1458–1471

infrared spectrum. The medium-pressure mercury lamp was surrounded with a water circulation jacket to absorb IR irradiation. The lamp exhibits broad range emission spectra (Figure 1b) with maxima in both the UV and the visible range. The lamp radiates 16% of the radiation in UV and the remaining in the visible region. The activity measurements were carried out in a photoreactor identical to that described above placed horizontally in a chamber close to a water-cooled medium pressure mercury vapor lamp. The typical reaction assembly under outer irradiation is shown in Figure 1c along with the irradiator.

2.3.4. Calculation of Apparent Quantum Efficiency of Photocatalytic Reaction under UV–Visible and Sunlight. The emission spectrum of a medium-pressure mercury lamp (Hg, Ace Glass Inc., 450 W) lamp was recorded in the wavelength range of 200–800 nm. For polychromatic light, the energy of a single photon was considered as the weighted average energy (E_a) of all of the photons in the range of 300–600 nm. For this, the contribution of photon of each wavelength λ_i (i varying from 300 to 600 nm) toward the total energy was calculated as

$$E_i\lambda_i = \frac{I_{\lambda i}}{I_{\text{tot}}} \times \frac{hc}{\lambda_i}$$

$$E_a = \sum_{300}^{450} E_i(\lambda_i)$$

Total light intensity incident at the sample position in horizontal geometry as shown in Figure 1c was measured using a calibrated lux meter (cal-Light 400). The intensity of the light source was measured using a calibrated precision lux meter (cal-Light 400). The lux meter was placed near the photo reactor, and the intensity was measured. It was also corrected for the reactor surface area exposed to light, assuming uniform intensity distribution, over the powder dispersed in the $2H_2O$ + methanol mixtures. The fraction of light intensity in the wavelength region between 300 and 600 nm only was considered for the calculation of quantum efficiency as the absorption of light above 600 nm was negligible. The incident light intensity in the range of 300–600 nm (E_m) was obtained by multiplying the total incident intensity by the ratio of the area in the 300–600 nm range to the total area of the emission profile. Finally, the quantum efficiency is given by the following expression:

$$\eta\ (\%) = \frac{2 \times \text{H}_2 \text{ yield}}{N} \times 100$$

where

$$N = \frac{E_m}{E_a}$$

Similarly, apparent quantum efficiency (AQE) was also calculated for the said photocatalytic reaction performed under a visible light lamp (emission spectrum given in Figure 1a) and sunlight.

2.4. First-Principles Theoretical Calculations. The self-consistent scalar relativistic TB-LMTO method within atomic sphere approximation (ASA) was employed, which also included the so-called "combined correction" term.[48−50] The potential is calculated using the density functional prescription under the local density approximation (LDA). Von Barth–Hedin parametrization of the exchange-correlation potential was employed for this purpose. The tetrahedron method of Brillouin zone (k-space) integration was used. Three structures, indium titanate (*Pnma*) and its modified form, that is, two supercells $(In,Nd)_2TiO_5$ containing, respectively, 12.5 and 18.75 atom % of Nd, occupying the In sites, were considered for this study. Spin-averaged LDA calculations were performed on the unit cell of In_2TiO_5 and these two 1 × 2 × 1 supercells, SC1 and SC2 corresponding to ITNd(2) and ITNd(3), respectively, containing 64 atoms (16 In, 8 Ti, 40 O atoms). It should be pointed out here that despite of the fact that the TB-LMTO-ASA method does not include spin–orbit effects, which may become important for heavier elements (Z > 50), the method is well-known to produce qualitative features of the band structure quite accurately.

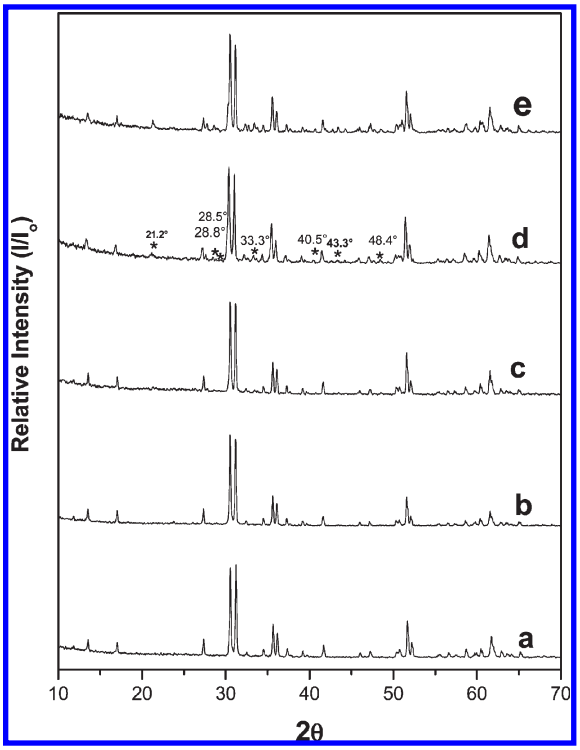

Figure 2. XRD patterns of $In_{2(1-x)}Nd_{2x}TiO_5$ samples synthesized by solid-state reaction (a–e) for different values of x. (a) ITNd(0), (b) ITNd(1), (c) ITNd(2), (d) ITNd(3), and (e) ITNd(4). *XRD peak at 2θ = 30.559° attributed to In_2TiO_5. #XRD peak at 2θ = 28.53° corresponds to $Nd_2Ti_2O_7$ phase, respectively.

3. RESULTS AND DISCUSSION

3.1. Phase Analysis by XRD. Table 1 lists the abbreviations and phases identified from XRD patterns of all of the $In_{2(1-x)}Nd_{2x}TiO_5$ ($0.0 \le x \le 0.2$) samples prepared by the solid-state method. Henceforth, in this Article we will use the abbreviated name of the samples. For completion of diffusion-controlled solid-state reaction, all samples were calcined at 1250 °C, resulting in well crystalline, stoichiometric, A_2TiO_5 ($A = In^{3+}, Nd^{3+}$)$_2$ single phased samples. Figure 2 shows the XRD patterns of $In_{2(1-x)}Nd_{2x}TiO_5$ as a function of x, where the XRD pattern of $x = 0$ composition matches that of orthorhombic ITNd(0) oxide. The unsubstituted, ITNd(0) is isostructural with In_2VO_5. It crystallizes as indium titanate oxide, In_2TiO_5, of orthorhombic space group, with unit cell of a = 0.7241 nm, b = 0.3427 nm, c = 1.4878 nm, cell volume = 0.3692 nm^3, and Z = 4 (JCPDS card no. 30-0640). The XRD patterns of Nd^{3+} substituted ITNd(0) compositions ($2x$ = 0.1, 0.2, 0.3, 0.4) are presented in curves

dx.doi.org/10.1021/jp207904k |J. Phys. Chem. C 2012, 116, 1458–1471

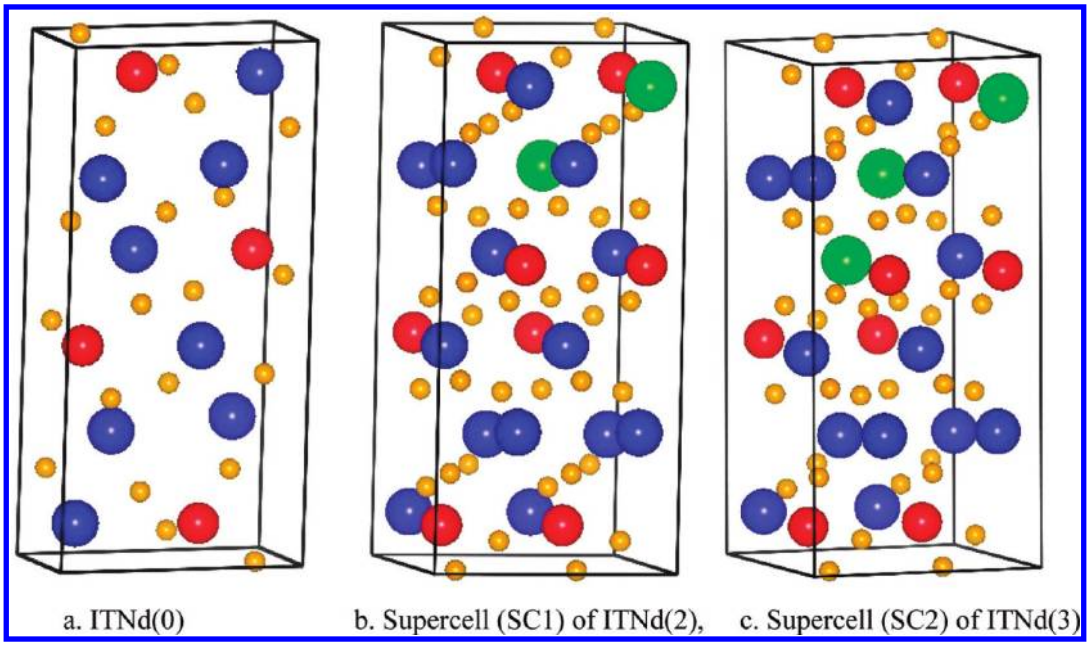

Figure 3. Unit cells of (a) ITNd(0) with In_2TiO_5 phase (*Pnma*) containing 32 atoms, (b) 1 × 2 × 1 supercell (SC1) of ITNd(2) containing 64 (16In + 8Ti + 40oxygen) atoms with two atoms of Nd substituting In sites and (c) 1 × 2 × 1 supercell (SC2) of ITNd(3) with three atoms of Nd substituting In sites. Blue, In; red, Ti; green, Nd; and orange, oxygen.

b−e of Figure 2. The lines due to reactant oxides are missing in these patterns, thus confirming the completion of the solid-state reaction. The indexed lattice parameters (POWDERX program[46]) and phases identified for each Nd substituted sample are mentioned in Table 1. XRD patterns shown in curves a−c reveal that up to 10% Nd^{3+} isovalent ion substitution in ITNd(0) has resulted in single-phasic compositions isomorphic to In_2TiO_5 phase. A secondary phase formation in ITNd(3) and ITNd(4) samples along with a major ITNd(0) phase is indicated by the presence of weak reflections at 2θ = 28.5°, 28.8°, 33.21°, marked as * in their XRD patterns (curves d,e). The lines corresponding to a new secondary phase were identified and attributed to the $Nd_2Ti_2O_7$ (JCPDS card no. 37-0942). Thus, A-site substitution by isovalent cation, Nd^{3+}, has induced a mixed phase formation beyond 10% of dopant comprised of both parent ITNd(0) and $Nd_2Ti_2O_7$ phases, whereas samples with ITNd(0), ITNd(1), and ITNd(2) compositions were single phase isomorphic to In_2TiO_5 phase. With the increase in the value of *x*, the cell volume increases (Table 1), which can be explained by inclusion of a larger cation, Nd^{3+} (0.0995 nm), in place of a relatively smaller size cation, In^{3+} (0.081 nm). Also, the peak width of the XRD lines corresponding to ITNd(0) phase in Nd^{3+} substituted samples is found to increase with increasing value of *x*, indicating the incorporation of Nd^{3+} in the lattice. For instance, the line width of 100% reflection corresponding to 203 plane of ITNd(0) unsubstituted sample was 0.68°, which increased to 0.8° and 0.96° in ITNd(3) and ITNd(4) samples (Figure 2d,e), respectively.

3.2. Crystal Structure and Modeling. Spin-averaged LDA calculations were performed on a unit cell of ITNd(0) and two 1 × 2 × 1 supercells, SC1 and SC2 (Figure 3), corresponding to $(In, Nd)_2TiO_5$ stoichiometry containing 64 atoms (16 In, 8 Ti, 40 O atoms). These 1 × 2 × 1 supercells were derived from the orthorhombic unit cell of ITNd(0) having 32 atoms (Figure 3a). In these two supercells, two (in SC1) and three (in SC2) indium

Table 2. Crystallite Size of $In_{2(1-x)}Nd_{2x}TiO_5$ Samples As Calculated from XRD Line Width Using the Scherrer Equation as a Function of Nd Content (2*x*) and Calcination Temperature

sample no.	sample	value of 2*x*	crystallite size (nm) of samples calcined at 1250 °C	surface area (m^2/g)
1	ITNd(0)	0.0	128−130	4.4
2	ITNd(1)	0.1	100−102	5.2
3	ITNd(2)	0.2	145−150	5.5

atoms were substituted by Nd, resulting in 12.5 and 18.75 atom % of Nd-substitution (Figure 3b,c) ,respectively. The Nd atoms can be substituted on In sites in a number of ways, leading to different configurations of the supercell. For the sake of brevity, we present here the results of the most stable configurations of SC1 and SC2 supercells. The basis set consisted of 4s, 4p, and 3d states of Ti; 5s, 5p states of In; 2p states of O; and 6s and 5d states of Nd, while the 5d, 4f states of In; 3s and 3d states of O; and 6p and 5f states of Nd were downfolded,[51] thereby restricting the size of the Hamiltonian and overlap matrices, without sacrificing the accuracy of the results. For empty spheres, only the 1s states were included, downfolding the p and d states. All calculations are fully converged with respect to number of *k*-points. Volume optimization from LDA calculations gave the equilibrium volume of ITNd(0) to be 370.172 $Å^3$ (*a* = 7.246 Å, *b*/*a* = 0.474, and *c*/*a* = 2.054), which agrees quite well with the experimental value of 377.63 $Å^3$. The equilibrium volumes of 1*2*1 supercells were calculated to be 741.709 $Å^3$ (*a* = 7.259 Å, *b*/*a* = 0.948, *c*/*a* = 2.054) for SC1 of ITNd(2); and 742.392 $Å^3$ (*a* = 7.266 Å, *b*/*a* = 0.948, *c*/*a* = 2.054) for SC2 of ITNd(4), revealing a slight increase in volume with Nd concentration. The qualitative analysis of XRD reflections (Figure 2) and their line width, indexing results (Table 1), along with theoretical calculations

dx.doi.org/10.1021/jp207904k |*J. Phys. Chem. C* 2012, 116, 1458–1471

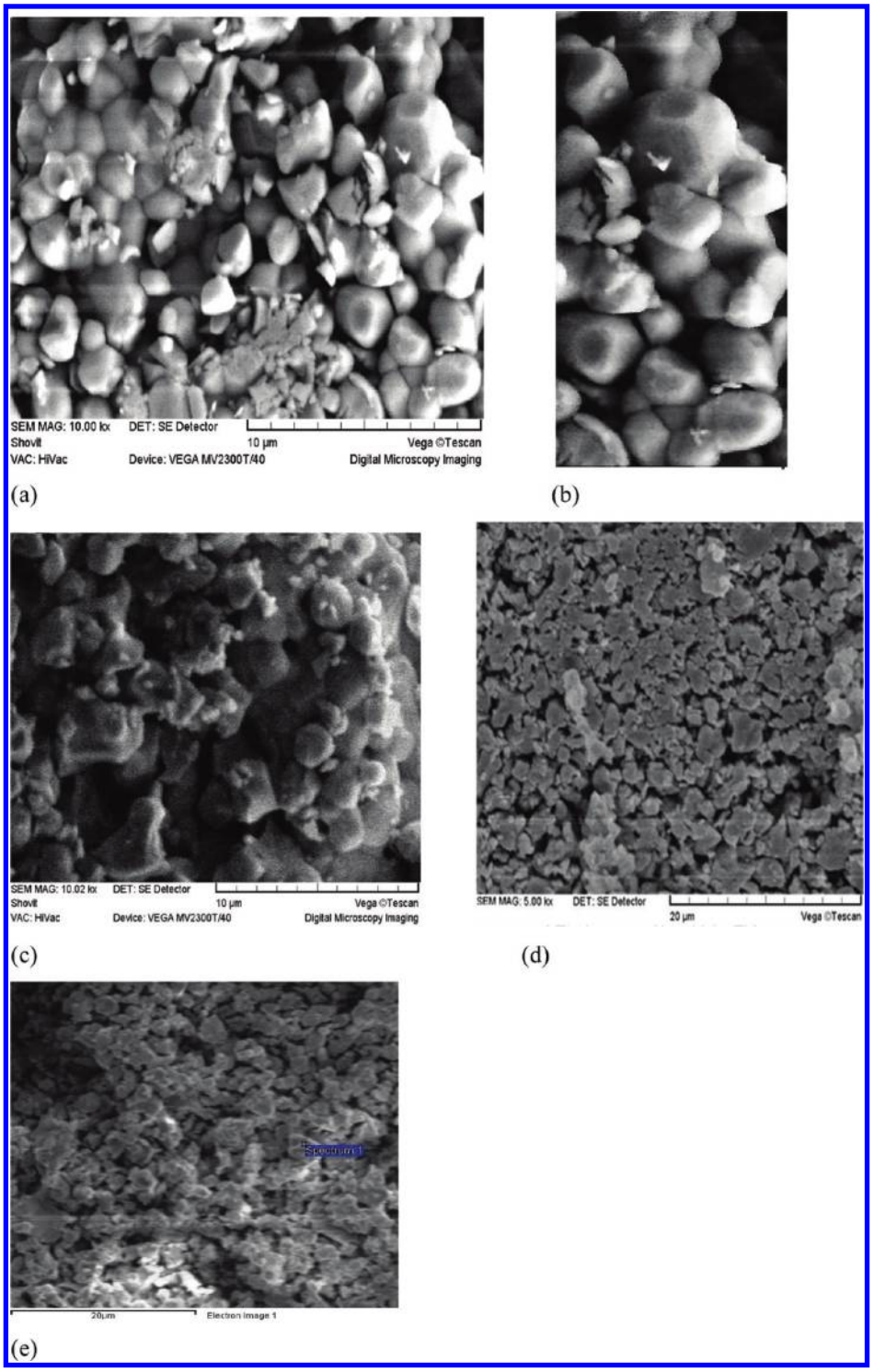

Figure 4. SEM image of (a) ITNd(0), (b) enlarged portion showing the faceted surface of ITNd(0), (c) ITNd(1), (d) ITNd(2), and (e) ITNd(4).

(Figure 3) demonstrates that the neodymium ion has been successfully incorporated into the lattice of ITNd(0), accompanied by the increase in cell volume.

3.3. Morphological Features by SEM, Particle Size, and N_2-BET Surface Area. The particle sizes of different samples as a function of Nd substitution are listed in Table 2. All samples are highly crystalline with large crystallite size (>100 nm) and very low N_2-BET surface area ($4-6\ m^2\ g^{-1}$). Table 2 includes exclusively single phasic samples obtained up to 10% Nd substitution. The growth in crystallite size with increase in calcination temperature for the representative sample, indium titanate, ITNd(0), is attributed to the sintering effects (Table 2).

Figure 4 shows the SEM images of ITNd(0) and substituted samples. Figure 4a shows the SEM micrograph of a typical sample of ITNd(0), where we can see the particles have a clear grain boundary with faceted structure, whereas Nd substitution

dx.doi.org/10.1021/jp207904k |J. Phys. Chem. C 2012, 116, 1458–1471

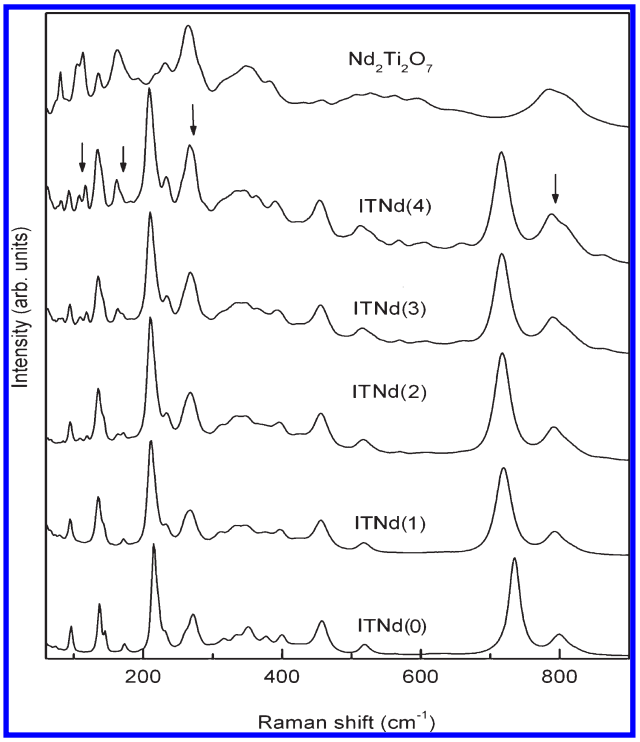

Figure 5. Raman spectra of $In_{2(1-x)}Nd_{2x}TiO_5$ samples as a function of Nd substitution: (a) ITNd(0), (b) ITNd(1), (c) ITNd(2), (d) ITNd-(3), and (e) ITNd(4). Arrow marks indicate the Raman modes due to $Nd_2Ti_2O_7$.

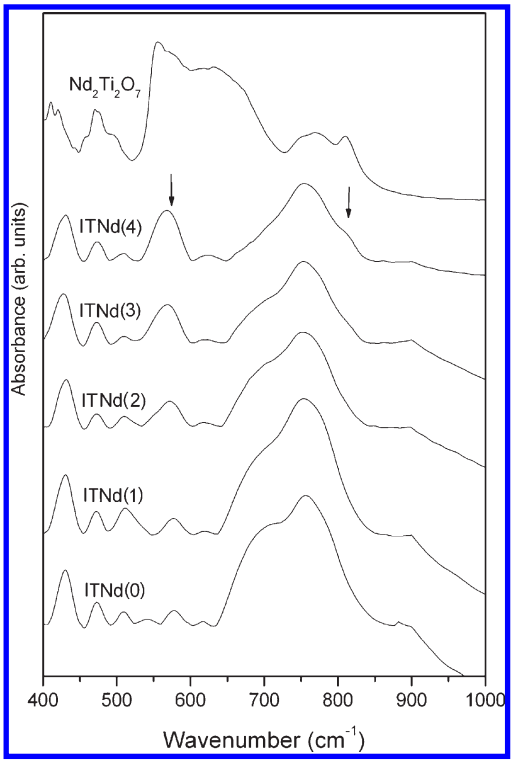

Figure 6. FTIR spectra of (a) ITNd(0), (b) ITNd(1), (c) ITNd(2), (d) ITNd(3), and (e) ITNd(4). Arrow marks indicate the appearance of modes due to $Nd_2Ti_2O_7$.

resulted in spherical particles without facets in Figure 4b−e. The particle size in each sample is observed to be in the micrometer range.

3.4. Raman and Infrared Spectroscopic Characterization. The compound ITNd(0) belongs to the space group D_{2h},[52] which has a center of inversion. So Raman and infrared spectra will give complementary information. There exists no report of Raman and infrared spectra of ITNd(0) in the literature. The Raman spectra of ITNd(0) and $In_{2(1-x)}Nd_{2x}TiO_5$ as a function of x are given in Figure 5. In comparison with the Raman spectra of Nd_2TiO_5,[52] which has the same structure, the strong mode at 735 cm^{-1} is attibuted to the symmetric stretching and the mode around 795 cm^{-1} to asymmetric stretching of the Ti−O bond in the TiO_5 square pyramid. With 5% Nd^{3+} substitution in indium titanate, that is, ITNd(1) sample, the symmetric stretching mode broadens and reduces in frequency by about 16 cm^{-1}. This is attributed to the larger ionic radius of Nd^{3+} due to which the cation potential experienced by the Ti−O is less. There is a slight downshift in frequencies of the bending modes as well as the external modes (modes below 300 cm^{-1}). The decrease in external mode frequencies could be due to the higher mass of Nd^{3+} as compared to In^{3+} ion. With increase in Nd content, say for ITNd(3), new peaks appear (indicated by arrow marks in Figure 5), which increase in intensity with Nd concentration; these new peaks are identified as due to $Nd_2Ti_2O_7$. IR adsorption spectra of $In_{2(1-x)}Nd_{2x}TiO_5$ and $Nd_2Ti_2O_7$ in the region 400−900 cm^{-1}, which is mainly due to the internal vibrations of TiO_5, are shown in Figure 6. IR spectra are observed to have intensity complementary to Raman spectra as the structure has a center of inversion. The modes stronger in Raman spectra will appear weaker in IR spectra and vice versa. Beyond 10% Nd substitution, the IR band at 570 cm^{-1} gains in intensity. The strong band at ∼750 cm^{-1} develops an asymmetry at the high frequency side (810 cm^{-1}). As compared to the IR spectrum of $Nd_2Ti_2O_7$, the additional features are attributed to the presence of separate phase $Nd_2Ti_2O_7$. The present results corroborate well with that of XRD and Raman spectroscopy in that the mixed phase, comprised of ITNd(0) and $Nd_2Ti_2O_7$ phases, is observed beyond 10% composition.

3.5. Photoluminescence Spectroscopy (PL). Figure 7 shows the photoluminescence spectra of the $In_{2(1-x)}Nd_{2x}TiO_5$ ($0.0 \leq 2x \leq 0.4$) samples. Here, we report PL spectra recorded at room temperature with the excitation wavelength employed at 230 nm. Although we could not get distinct peaks corresponding to different transitions, a broad asymmetric peak in the wavelength region from 300 to 600 nm has been observed in PL spectra of all samples. Curve a shows a broad asymmetric peak centered at ∼386 nm accompanied by a shoulder at ∼367 nm and another at ∼555 nm observed in the PL spectra of unsubstituted ITNd(0). The band edge emission observed at ∼386 nm in PL spectra of ITNd(0) is broad due to its indirect band gap.[53] The second broad band at ∼555 nm due to trap state emission is weak in ITNd(0). As a result of Nd doping, band edge emission has considerably intensified and shifted to 364 nm as observed in Figure 7 b,c. Band structure calculations reveal a direct band gap in the ITNd(2) sample, which is responsible for intensifying the band edge emission in the ITNd(2) sample. This also suggests that impurity 4f and 5d levels due to the presence of Nd ions contribute in band edge emission. Whereas with further Nd substitution, for ITNd(3) and ITNd(4) samples (curves d,e), the intensity of band edge emission has considerably decreased and flattened. Segregation of separate phase $Nd_2Ti_2O_7$ beyond 10%

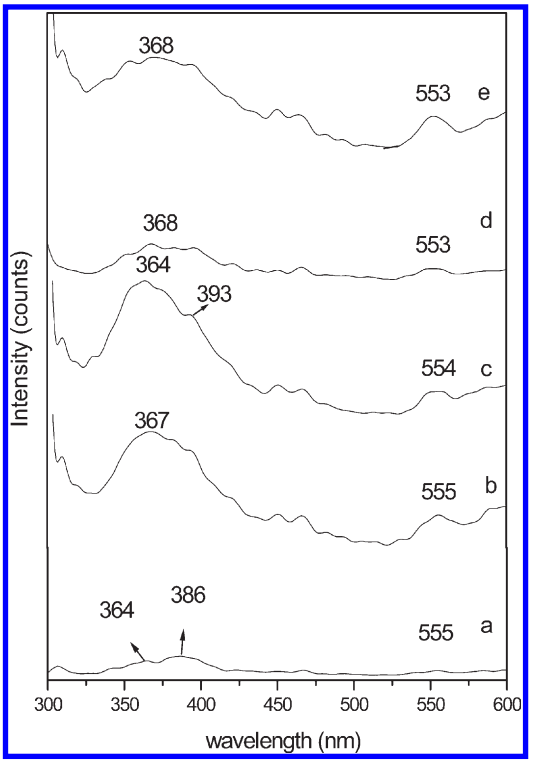

Figure 7. Photoluminiscence spectra of $In_{2(1-x)}Nd_{2x}TiO_5$ samples with varying compositions (a) ITNd(0), (b) ITNd(1), (c) ITNd(2), (d) ITNd(3), and (e) ITNd(4).

may quench the band edge emission, while the trap state emission band at 555 nm is almost constant for all Nd substituted samples (curves b−e) relative to that of the undoped sample (curves a). For indium titanate, the trap state emission is quite weak, whereas its intensity increases up to ITNd(2) sample and is constant with further increase in Nd contents.[54,55] The intensity of the 555 band in the Nd-doped samples is determined by the number of free defects, relative to those surface defect sites that are bound with Nd ions, which would otherwise trap excited-state electrons and prevent fluorescence.[54−56]

3.6. UV−Visible Reflectance Spectroscopy. The metal ion substitution affects the electronic structure of the semiconducting photocatalysts, which is manifested in their UV−vis spectra. Figure 8 shows the UV−visible spectrum of $In_{2(1-x)}Nd_{2x}TiO_5$ samples. These spectra illustrate the light absorption properties of the $In_{2(1-x)}Nd_{2x}TiO_5$ (x = 0.0−0.5) series, showing that the visible absorption spectra of these compounds are characteristic of photocatalysts able to respond to visible light. The band gap is likely to occur between the top of the oxygen 2p band and the bottom of the Ti 5d (t_{2g}) band. Curve a shows the absorption spectrum of ITNd(0), with the absorption band edge from 300 to 500 nm corresponding to an optical gap of 3.02 eV, which is in the UV region. The position of the absorption edge was almost constant for ITNd(0) and ITNd(1), but has shifted to higher wavelengths for further Nd substituted samples (curves c−e) revealing that the Nd^{3+} substitution has enabled the sample to absorb in the visible region. Besides the band gap transition, several sharp absorptions in the visible and IR region at 529.5, 588.5, 741, 802, 866, and 879 nm were observed in the spectra of Nd substituted samples as shown in Figure 8. The intensity of

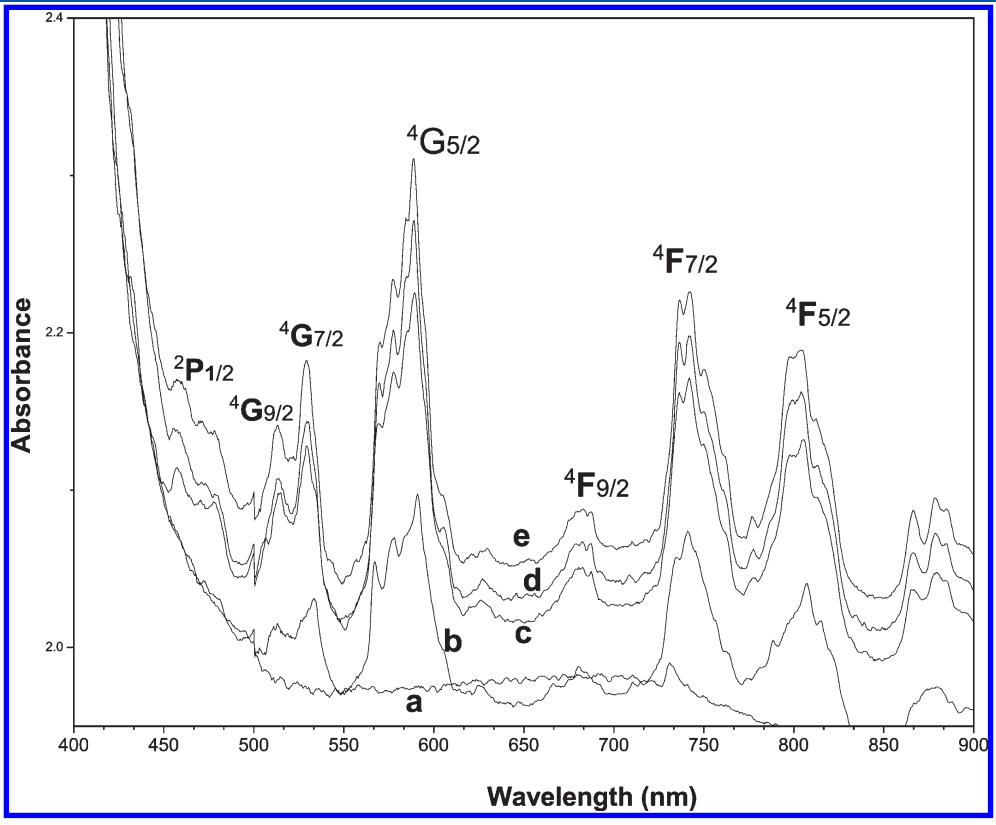

Figure 8. Difuse reflectance UV−visible spectra of (a) ITNd(0), (b) ITNd(1), (c) ITNd(2), (d) ITNd(3), and (e) ITNd(4). Symbols for each absorption show the excited states of isolated Ln 4f. The ground states are: Nd, $^4I_{9/2}$.

dx.doi.org/10.1021/jp207904k | J. Phys. Chem. C 2012, 116, 1458–1471

Table 3. AQE and H_2 Yield (μmol/h) Obtained Photocatalytically over $In_{2(1-x)}Nd_{2x}TiO_5$ Samples Irradiated with Different Light Sources

		H_2 yield (μmol/h)			
		sunlight	visible light	UV−visible light	
sample no.	sample	0.1 g of photocatalyst + 10 mL of water + 5 mL of methanol, irradiated under sunlight from 1030 to 1630 h IST	0.1 g of photocatalyst + 10 mL of water + 5 mL of methanol, irradiated under flux of ~10^{17} photons/s	0.1 g of photocatalyst + 10 mL of water + 5 mL of methanol, irradiated under flux of the ~10^{17} photons/s	apparent quantum efficiency (η, %)
1	ITNd(0)	0	0	13.8	0.86%
2	ITNd(1)	0.03	0.08	17.2	1.07%
3	ITNd(2)	0.9, η = 0.09	1.9, η = 0.1	38.3	2.3%
4	ITNd(3)	0	0	22.8	1.36%
5	ITNd(4)	0	0	15.8	0.95%
6	Pt/ITNd(2)			75.0	4.5%

these peaks was found to increase with the increase in Nd content (Figure 8b−e). The positions of these absorptions are in accord with the internal 4f transitions observed in corresponding Ln(3+) complexes, which give rise to narrow absorption bands quite unlike band gap transitions.[57] The localized 4f levels in the present systems are considered to lie within the band gap. However, it should be noted that several absorptions overlapping the onset of the absorption edge in the Nd systems are not ascribed to internal transitions. In particular, a much broader absorption in the range 300−400 nm suggests possible charge-transfer transitions between Nd 4f and other bands.

Density of states and band structure calculations for ITNd(0) and ITNd(2), using first principles, are given in section 3.8, which shows Nd 4f and 5d orbitals contribute in the band structure of Nd substituted oxides and explains that these optical transitions are arising from its electronic structure.

3.7. Photoactivity. Unsubstituted ITNd(0) and Nd substituted, ITNd(2x) (2x = 0.1, 0.2, 0.3, and 0.4), samples were evaluated for photocatalytic activity for H_2 generation under different conditions. Table 3 lists typical H_2 yields generated from each sample, when irradiated with various light sources under identical conditions. Typically, the photoactivity tests were carried out in three different lights: (a) sunlight, (b) visible light (emission spectrum shown in Figure 1a), and (c) UV−visible light (emission spectrum shown in Figure 1b). Under sunlight irradiation among all samples, maximum photoactivity was observed over ITNd(2), ITNd(1) was photoactive but with lesser yield, and ITNd(3) and ITNd(4) along with unsubstituted ITNd(0) have not shown any photoactivity (Table 3). Figure 9 shows the typical yields of hydrogen (μmoles) obtained over 0.1 g of ITNd(2) sample irradiated under sunlight and visible light. ITNd(2) has also shown maximum photoresponse in visible light and generated 11.2 μmol of H_2 as compared to other photocatalysts (Table 3). Both single phase compositions ITNd(1) and ITNd(2) responded toward sunlight, whereas biphasic and unsubstituted In_2TiO_5 samples were inactive. Considering that all samples were not responding to sunlight/visible, therefore their photocatalytic properties were also investigated under UV−visible irradiation (Table 3). Figure 10A shows the time-dependent photocatalytic H_2 evolution over these Nd^{3+} substituted indium titanate semiconductors under UV−visible light. All samples were found to be photoactive with the maximum photocatalytic conversion obtained over the ITNd(2) sample at the rate of ~38.3 μmol/h. The decreasing order of catalytic

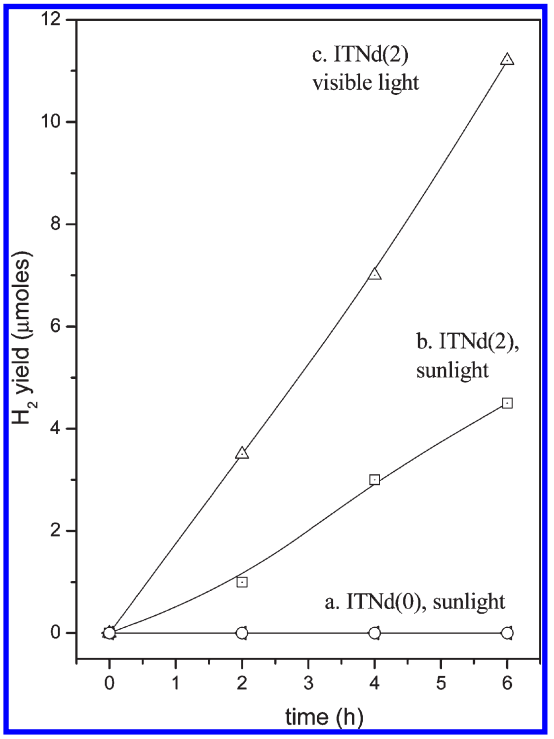

Figure 9. Typical yields of hydrogen obtained under sunlight and visible light source over ITNd(2). (a) For comparison, unsubstituted ITNd(0) under sunlight, (b) ITNd(2) under sunlight, and (c) ITNd(2) visible light. Reaction conditions: 0.1 g of catalyst, 10 mL of distilled water, 5 mL of methanol. Light source: (a) Sunlight for 6 h during afternoon (1030 to 1630 h IST); (b) visible, water cooled medium-pressure mercury lamp that emits wavelengths longer than 400 nm (λ_{max} = 536 nm) as shown in Figure 1a.

activity as obtained from Figure 10B is as follows: ITNd(2) > ITNd(3) > ITNd(1) > ITNd(4) > ITNd(0) under UV−visible light.

The dependence of photoactivity on experimental conditions was also investigated. The influence of atmosphere inside photoreactor on photocatalytic activity was monitored by exposing the reaction mixture (photocatalyst + water + MeOH) to three different atmospheres during irradiation: (a) an inert atmosphere of argon gas, (b) reactor evacuated before irradiation, and (c) reactor evacuated and then filled with 0.3 atm of argon gas

dx.doi.org/10.1021/jp207904k | J. Phys. Chem. C 2012, 116, 1458–1471

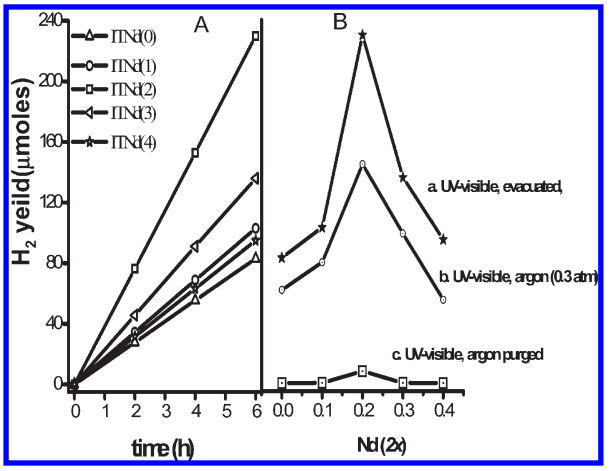

Figure 10. Photoactivity of all $In_{2(1-x)}Nd_{2x}TiO_5$ samples ($0.0 \leq x \leq 0.4$) as a function of (A) irradiation time and (B) different experimental conditions: (a) UV−visible, evacuated before irradiation, (b) UV−visible, argon (P = 0.3 atm), and (c) UV−visible argon (P = 1 atm). Reaction conditions: 0.1 g of catalyst, 10 mL of distilled water, 5 mL of methanol. Light source: UV−visible medium-pressure mercury lamp, surrounded with a water circulation jacket to absorb IR irradiation.

before irradiation. The amount of hydrogen generated over all of the samples under different experimental conditions is shown in Figure 10B. It is evident from Figure 10B that the hydrogen yield increases as the pressure inside the photoreactor decreases. Maximum H_2 yield was obtained photocatalytically over ITNd-(2) sample when the reaction mixture was evacuated before irradiation. Photocatalytic decomposition of water was favored most when the reaction mixture was irradiated under evacuated conditions as compared to inert or partial atmoshpheres. The same trend was observed for all of the samples as shown in Figure 10B. Oxygen-free conditions favor photocatalytic activity as oxygen acts as e-scavenger, and also it gets photoadsorbed on the photocatalysts and blocks the active sites for the reaction. Thus, evacuation before irradiation is the most favorable condition to generate maximum photocatalytic H_2 from water. Also, the electrochemical potential of H_2 evolution shifts to the positive direction, with increasing ambient pressure according to the Nernst equation.[58] It was also suggested that removal of other photoadsorbed species onto the semiconductor particles is facilitated under reduced pressures; hence, the photocatalytic yield of H_2 increases.[58−60] Under various light sources, sunlight, visible, as well as UV−visible light, ITNd(2) was found to be the most photoactive sample.

Figure 11 shows the H_2 yield obtained photocatalytically as a function of time for ITNd(1) sample. The irradiation time was also intercepted with dark period during which the rise in the H_2 yield was not observed. Here, H_2 yield increased steadily and linearly with irradiation time and was stopped when the light was turned off. Thus, it could be concluded that H_2 evolution over Nd/In/Ti/O catalysts occurred photocatalytically. In addition to different reaction conditions, the effect of cocatalyst on the photoactivity was also monitored. Figure 12 reveals that loading of 1% Pt as cocatalyst on ITNd(2) catalyst enhances the H_2 yield more than 2-fold to ∼4600 μmol/g. The estimated apparent quantum efficiency (AQE) values over all samples under different sources of light are listed in Table 1. Apparent quantum efficiencies of ITNd(2) were 2.3%, 0.09%, and 0.1% when irradiated with wavelengths more than 250 nm (UV−visible),

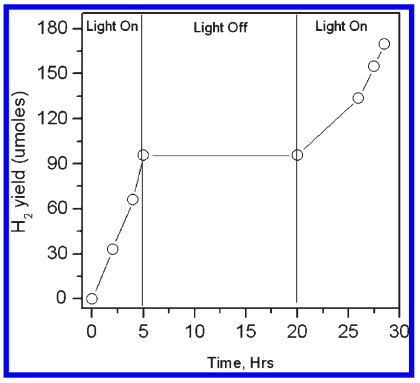

Figure 11. Time-dependent photocatalytic activity ITNd(1). H_2 generated photocatalytically when light was shined. During the dark period, there was no H_2 generation. Reaction conditions: 0.1 g of catalyst, 10 mL of distilled water, 5 mL of methanol. Light source: UV−visible medium-pressure mercury lamp (Hg, Ace Glass Inc., 450 W) surrounded with a water circulation jacket to absorb IR irradiation.

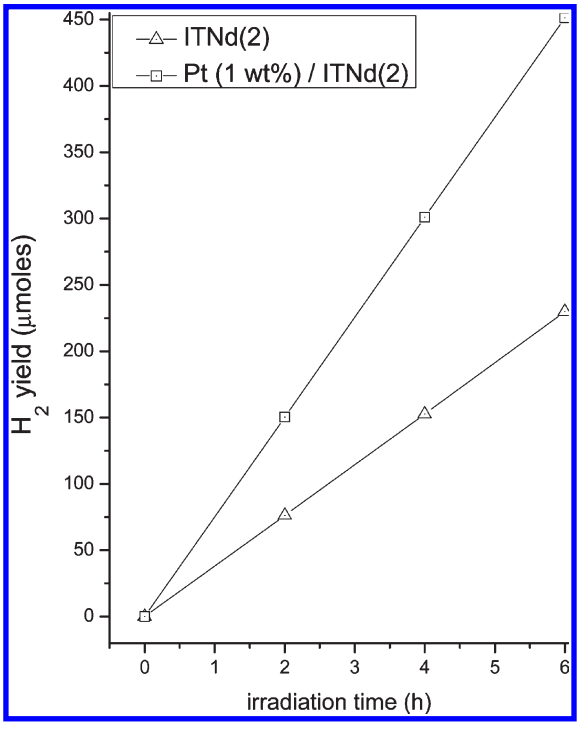

Figure 12. Photoactivity of ITNd(2) sample loaded with and without Pt cocatalyst. Reaction conditions: 0.1 g of catalyst, 10 mL of distilled water, 5 mL of methanol. Light source: UV−visible medium-pressure mercury lamp (Hg, Ace Glass Inc., 450 W) surrounded with a water circulation jacket to absorb IR irradiation.

wavelengths more than 400 nm (visible), and sunlight, respectively. The apparent quantum efficiency with and without catalyst irradiated with different light sources for the ITNd(2) sample is shown in Figure 13. It can be seen that the apparent quantum efficiency decreases with increase in wavelength, and the spectrum resembles the absorption spectrum of this sample. These results show that the reaction occurred photocatalytically and the sample is visible light active. Maximum AQE of 2.3% is obtained with ITNd(2) among all samples, increases by 2-fold in the presence of cocatalyst, and is found to be 4.5% for Pt/ITNd(2) sample (Figure 13).

dx.doi.org/10.1021/jp207904k |J. Phys. Chem. C 2012, 116, 1458–1471

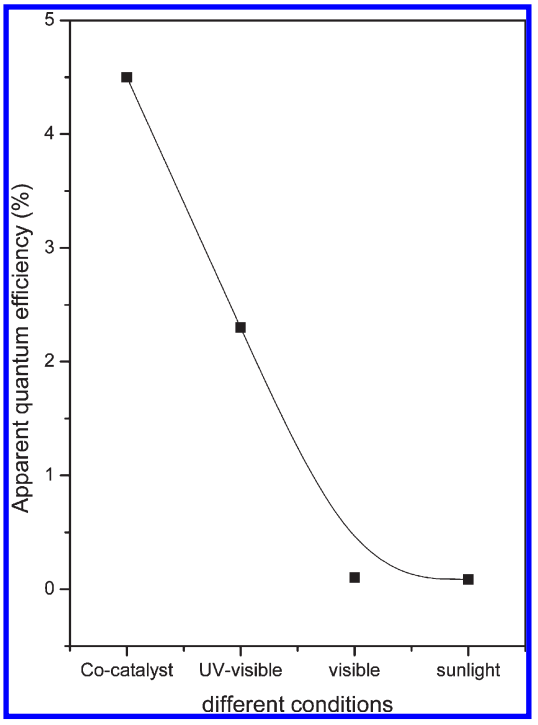

Figure 13. Apparent quantum efficiencies (%) achieved with ITNd(2) sample for photocatalytic hydrogen generation when loaded with cocatalyst Pt in UV−visible light, and without cocatalyst irradiated under sunlight, visible, and UV−visible light. Details of AQE calculations are mentioned in section 2.3.4, which takes care of fluxes of different light sources.

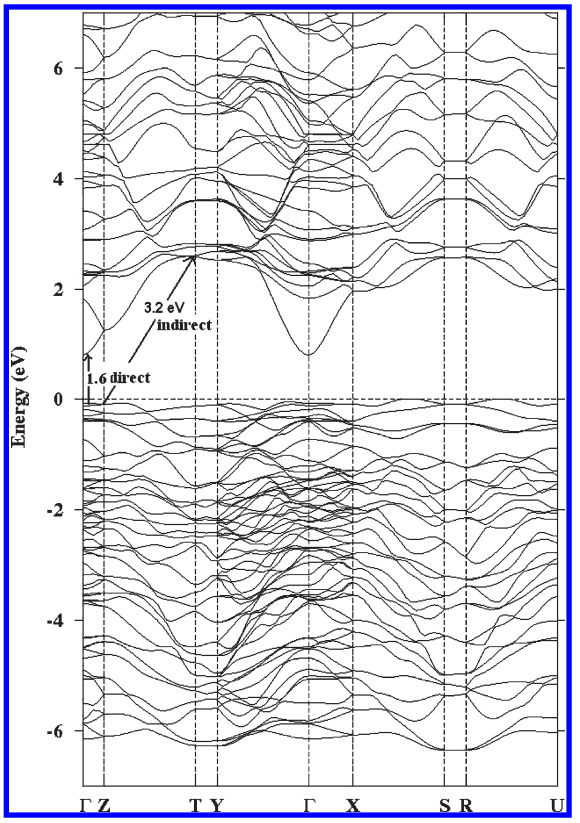

Figure 14. Band structure of ITNd(0) along high-symmetry Γ(0,0,0), X(0.25,0,0), Y(0,0.5,0), Z(0,0,0.125), S(0.25,0.5,0), R(0.25,0.5,0.125), T(0,0.5,0.125), and U(0.25,0.0,0.125) directions.

3.8. Electronic Structure. The electronic structures of ITNd-(0), ITNd(2), and ITNd(3) samples were calculated using TB-LMTO code to clarify the distribution of valence states of Ti, In, O atoms near the Fermi level and to understand the role of Nd, ions in modifying the band structure of ITNd(0), thereby enhancing H_2 yield in visible range. Figures 14 and 16 show the calculated band structures, respectively, of ITNd(0) and supercell SC1 having 12.5 atom % Nd substituting indium sites, corresponding to ITNd(2) sample, along a few high-symmetry directions; while Figures 15 and 17 show total as well as site- and L-projected partial density of states (DOS) for ITNd(0) and ITNd(2), respectively. For the sake of brevity, calculated band structure and DOS of 18.75 atom % Nd doped supercell, SC2 corresponding to sample ITNd(3), are not shown as these are similar to those of the ITNd(2). As expected, the LDA band structure of ITNd(0) (Figure 14) shows all of the features identical to those reported by Wang et al.[44] using the same TB-LMTO method. The lowest unoccupied state (LUMO) is found at Γ-point (0,0,0), whereas the highest occupied state (HOMO) is found between points S and X; Y and Γ; R and U in the valence band, but not at Γ-point as shown in Figure 14. Thus, ITNd(0) has indirect band gap between the LUMO and HOMO as revealed from Figure 14. There are two indirect bands in the range of 1.6−3.0 eV above the Fermi level, which mainly consists of In 5s orbitals. The calculated E_g (band gap) of 1.6 eV is not consistent with the optical band gap (3.02 eV). The valence band consists of mainly O-2p, Ti-3d, and In-5p and In-4d states (Figure 15), while the conduction band is comprised of Ti-3d, In-5s, and In-5p states. The In-4d states in the valence band show a sharp peak near the Fermi level representing their localized

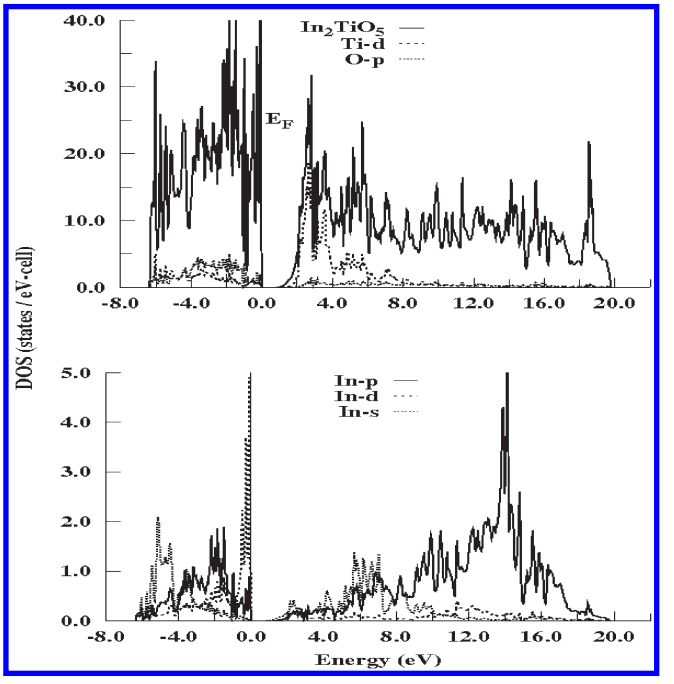

Figure 15. Total and site- and angular momentum-projected partial density of states for ITNd(0) showing the valence band to be mainly composed of O-p, Ti-d, and In-p,d states.

nature. The strong optical transitions are due to flat bands from valence band to conduction band (Figure 14), and these are

dx.doi.org/10.1021/jp207904k | J. Phys. Chem. C 2012, 116, 1458–1471

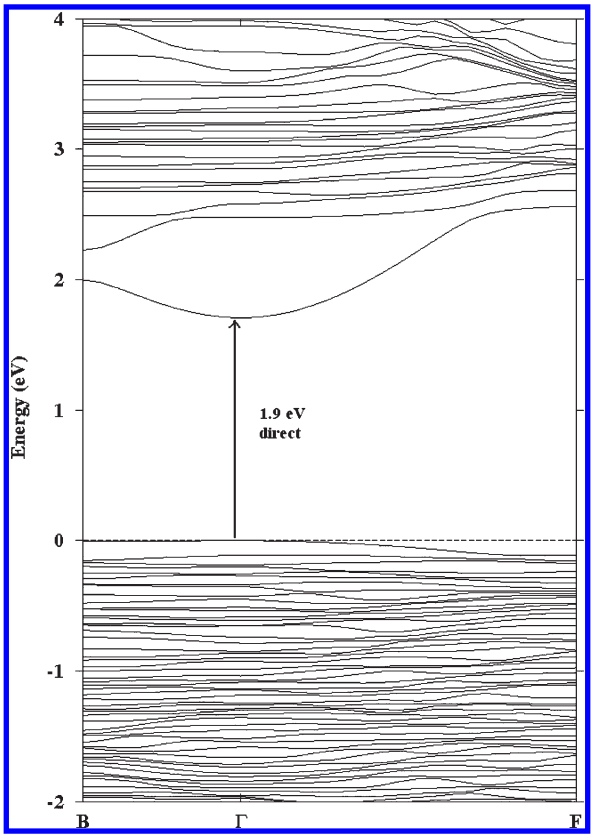

Figure 16. Band structure of ITNd(2) (SC1) along high-symmetry Γ(0,0,0), B(0.25,0,0), and F(0,0.5,0) directions.

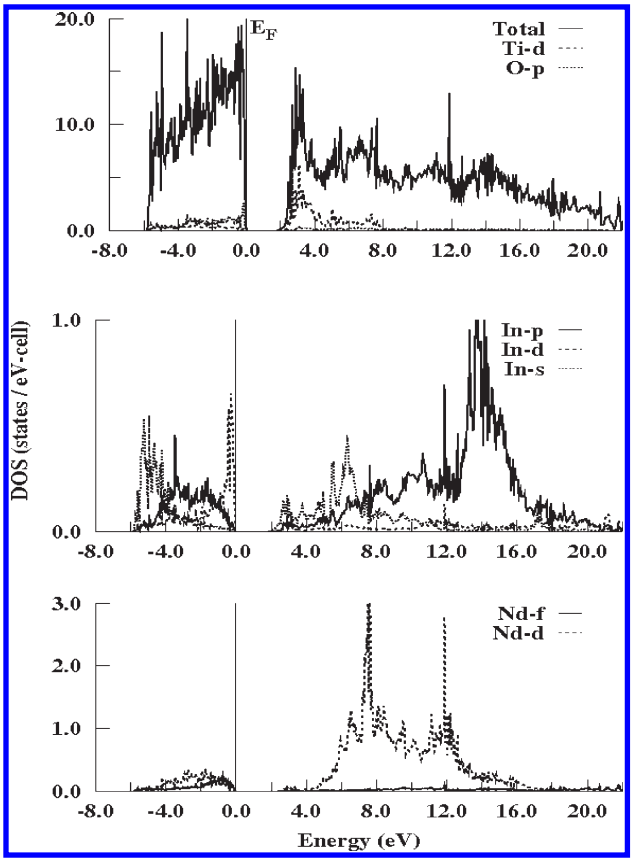

Figure 17. Total and site- and angular momentum-projected partial density of states for ITNd(2) supercell, SC1, showing the effect of Nd-d,f states on the band gap near the Fermi energy.

found along the S to X point and the R to U point and the T to Y-point and the R to S-point. The transition from highest occupied states to the unoccupied states between T and Y or between S and R, respectively, exhibits a gap about 3.20 eV, which is closer to the observed value (3.02 eV). The O 2p states contribute considerably to the density of states near the Fermi level, whereas the Ti 3d and 4s just make the contributions above the Fermi level. In 5s, states are of large dispersion with rather small DOS; thus the indirect band gap of 1.6 eV is not a flat band to flat band transition, and hence is less probable. Evidently, this transition manifests itself as a shoulder in the experimental optical spectrum. Band calculations on unsubstituted ITNd(0) reveal that the large dispersion of In 5s states and the optical indirect transition are in favor of photon energy storage and electron−hole separation to benefit the photocatalytic activity of ITNd(0). This model study is also useful in understanding the performance of similar photocatalysts.

To the best of our knowledge, first-principles electronic structure calculations on Nd-doped In_2TiO_5, that is, ITNd(2), have not been attempted earlier. We have employed the same methodology for calculating the band structure of ITNd(2). It should be pointed out here that despite the fact that the TB-LMTO-ASA method does not include spin−orbit effects, which may become important for heavier elements ($Z > 50$), the method is well-known to produce qualitative features of the band structure quite accurately. On substitution of Nd at the In site in ITNd(0) corresponding to supercell SC1 of ITNd(2), the band structure (Figure 16) exhibits a direct band gap between the lowest unoccupied and the highest occupied states at the Γ-point. The valence band now also consists of the Nd-d, f states mixed with O-p, In-p, d, Ti-d states (Figure 17). The flat bands in the valence as well as conduction bands are found between the Γ- and B-points and close to the F-point. The minimum direct band gap of about 1.9 eV is observed along the Γ-point between a flat band in the valence band and that in the conduction band, while the maximum direct band gap is about 2.6 eV occurring at the F-point. The transitions between these states are responsible for improved optical properties of Nd-doped ITNd(0) because of enhanced transition probabilities arising from flat bands. The Fermi level energy increases from ITNd(0) to Nd substituted, ITNd(2) sample from −2.318 eV (0.1705 ryd) to −1.4892 eV (−0.1095 ryd) respectively. Thus, the valence band is raised toward the conduction band by an energy of 0.82 eV in ITNd-(2)sample as compared to the ITNd(0) sample as shown in Figure 18. The lowering of band gap in ITNd(2) sample is attributed to an increase in energy of the valence band along with a decrease in conduction band also. The valence band in ITNd-(0) mostly consists of O2p and In 5p states, whereas in the Nd substituted sample the Nd 5d and 4f states also contribute in the valence band. In contrast to the ITND(0), it was revealed that the band gaps of ITNd(2) were 1.2 eV lower than ITNd(0) because the Nd 4f and 5d states made the valence band at less negative levels than the O2p orbitals by 0.82 eV. The ITNd(2) is single phasic with crystal structures isomorphic to indium titanate (ITNd(0)) structure. However, the intermixing of Nd 5d and 4f orbitals with O 2p orbitals in ITNd(2) sample has increased the energy of valence band. Also, conduction bands of ITNd(2) samples are slightly lower in energy than those of

dx.doi.org/10.1021/jp207904k | J. Phys. Chem. C 2012, 116, 1458–1471

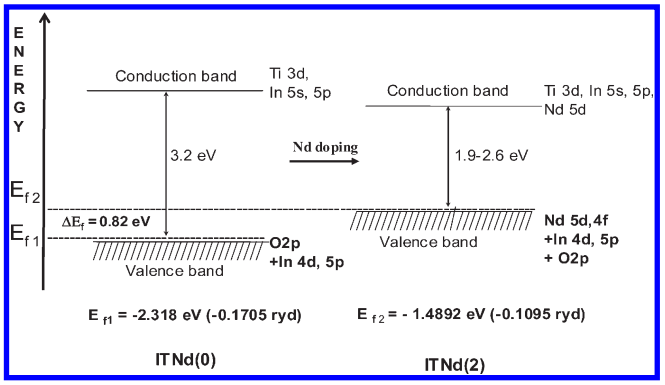

Figure 18. Modified band structure of ITNd(2) photocatalyst semiconductors.

ITNd(0), thus resulting in a net lowering of band gap by ~1.0 eV (Figure 18). It is to be noted that indirect band gaps between flat bands in the valence and conduction bands are much larger. Thus, Nd is one of the elements that is able to make a valence-band position higher than O 2p orbitals. Similarly, Kato et al.[61] reportedly have shown that a hybrid orbital of Ag 4d and O 2p formed a valence band at a more negative level than O 2p orbitals using the plane-wave-based density functional method, when they were investigating the photophysical and photocatalytic properties of perovskite-type materials $AgMO_3$ (M: Ta and Nb). As a result, they found that the band gaps of $AgTaO_3$ and $AgNbO_3$ were 3.4 and 2.8 eV, respectively, smaller than the band gaps of $NaTaO_3$ (4.0 eV) and $NaNbO_3$, even if the crystal structures of $AgMO_3$ were similar to those of $NaMO_3$. Similarly, for the ITNd(2) sample, band structure reveals that Nd 4f and 5d orbitals made the valence bands at more negative levels than the O 2p orbitals.

4. CONCLUSIONS

Isovalent Nd^{3+} ion substitution at the A-site in In_2TiO_5 has considerably enhanced H_2 yield and photoresponse in sunlight as well as in visible light irradiation. The favorably modified electronic structure on Nd doping is responsible for considerable rise in photoactivity of Nd substituted samples as compared to unsubstituted In_2TiO_5. It has been found that Nd is one of the elements that are able to make a valence-band position higher than O 2p orbitals. Thus, Nd substitution led to lowering in activation barrier for the said reaction as compared to unsubstituted indium titanates. This is noteworthy information needed to design new visible light-driven photocatalysts.

AUTHOR INFORMATION

Corresponding Author

*Tel.: 91 22 25592288. Fax: 9122 25505151. E-mail: mrinalr@barc.gov.in, mrinalpai9@gmail.com.

REFERENCES

(1) Linsebigler, A. L.; Lu, G.; Yates, J. T., Jr. *Chem. Rev.* **1995**, *95*, 735.
(2) Esswein, A. J.; Nocera, D. G. *Chem. Rev.* **2007**, *107*, 4022–4047.
(3) Maeda, K.; Domen, K. *J. Phys. Chem. C* **2007**, *111*, 7851.
(4) Kudo, A.; Miseki, Y. *Chem. Soc. Rev.* **2009**, *38*, 253–278.
(5) Domen, K.; Naito, S.; Soma, M.; Onishi, T.; Tamaru, K. *J. Chem. Soc., Chem. Commun.* **1980**, 543–544.
(6) Lehn, J. M.; Sauvage, J. P.; Ziessel, R. *Nouv. J. Chim.* **1980**, *4*, 623–627.
(7) Domen, K.; Naito, S.; Onishi, T.; Tamaru, K. *Chem. Phys. Lett.* **1982**, *92*, 433–434.
(8) Inoue, Y.; Kubokawa, T.; Sato, K. *J. Chem. Soc., Chem. Commun.* **1990**, 1298–1299.
(9) Inoue, Y.; Niiyama, T.; Asai, Y.; Sato, K. *J. Chem. Soc., Chem. Commun.* **1992**, 579–580.
(10) Iwase, A.; Kato, H.; Kudo, A. *Catal. Lett.* **2006**, *108*, 7.
(11) Ikeda, S.; Hara, M.; Kondo, J. N.; Domen, K.; Takahashi, H.; Okubo, T.; Kakihana, M. *J. Mater. Res.* **1998**, *13*, 852–855.
(12) Shibata, M.; Kudo, A.; Tanaka, A.; Domen, K.; Maruya, K.; Onishi, T. *Chem. Lett.* **1987**, *16*, 1017.
(13) Takata, T.; Furumi, Y.; Shinohara, K.; Tanaka, A.; Hara, M.; Kondo, J. N.; Domen, K. *Chem. Mater.* **1997**, *9*, 1063–1064.
(14) Kudo, A.; Kato, H. *Chem. Lett.* **1997**, *26*, 867–877.
(15) Yao, W.; Ye, J. *Chem. Phys. Lett.* **2007**, *435*, 96.
(16) Mitsuyama, T.; Tsutsui, A.; Hara, T.; Ikeue, K.; Machida, M. *Bull. Chem. Soc. Jpn.* **2008**, *81*, 401.
(17) Yuan, Y.; Zheng, J.; Zhang, X.; Li, Z.; Yu, T.; Ye, J.; Zou, Z. *Solid State Ionics* **2008**, *178*, 1711.
(18) Kadowaki, H.; Saito, N.; Nishiyama, H.; Inoue, Y. *Chem. Lett.* **2007**, *36*, 440.
(19) Sakata, Y.; Matsuda, Y.; Yanagida, T.; Hirata, K.; Imamura, H.; Teramura, K. *Catal. Lett.* **2008**, *125*, 22.
(20) Hosogi, Y.; Kato, H.; Kudo, A. *J. Mater. Chem.* **2008**, *18*, 647.
(21) del Valle, F.; Ishikawaa, A.; Domena, K.; Villoria de La Mano, J. A.; Sanchez-Sanchez, M. C.; Gonzalez, I. D.; Herreras, S.; Mota, N.; Rivas, M. E.; lvarez Galvn, M. C.; Fierro, J. L.; Navarro, G. R. M. *Catal. Today* **2009**, *143*, 51.
(22) Kudo, A.; Tsuji, I.; Kato, H. *Chem. Commun.* **2002**, 1958.
(23) Zheng, N.; Bu, X.; Vu, H.; Feng, P. *Angew. Chem.* **2005**, *117*, 5433.
(24) Sayama, K.; Mukasa, K.; Abe, R.; Abe, Y.; Arakawa, H. *Chem. Commun.* **2001**, 2416.
(25) Machida, M.; Miyazaki, K.; Matsushima, S.; Arai, M. *J. Mater. Chem.* **2003**, *13*, 1433.
(26) Machida, M.; Mitsuyama, T.; Ikeue, K.; Matsushima, S.; Arai, M. *J. Phys. Chem. B* **2005**, *109*, 7801.
(27) Kim, J.; Hwang, D. W.; Kim, H. G.; Bae, S. W.; Ji, S. M.; Lee, J. S. *Chem. Commun.* **2002**, 2488.
(28) Yao, W. F.; Xu, X. H.; Wang, H.; Zhou, J. T.; Yang, X. N.; Zhang, Y.; Shang, S. X.; Huang, B. B. *Appl. Catal., B: Environ.* **2004**, *52*, 109.
(29) Hwang, D. W.; Lee, J. S.; Li, W.; Oh, S. H. *J. Phys. Chem. B* **2003**, *107*, 4963.
(30) Hwang, D. W.; Kim, H. G.; Lee, J. S.; Kim, J.; Li, W.; Oh, S. H. *J. Phys. Chem. B* **2005**, *109*, 2093.
(31) Hwang, D. W.; Kim, H. G.; Jang, J. S.; Bae, S. W.; Ji, S. M.; Lee, J. S. *Catal. Today* **2004**, *93*, 845.
(32) Hwang, D. W.; Kim, H. G.; Lee, J. S.; Kim, J.; Li, W.; Oh, S. H. *J. Phys. Chem. B* **2005**, *109*, 2093–2102.
(33) Kim, H. G.; Hwang, D. W.; Lee, J. S. *J. Am. Chem. Soc.* **2004**, *126*, 8912–8913.
(34) Kudo, A.; Hijii, S. *Chem. Lett.* **1999**, *28*, 1103.
(35) Shimodaira, Y.; Kato, H.; Kobayashi, H.; Kudo, A. *J. Phys. Chem. B* **2006**, *110*, 17790.
(36) Maeda, K.; Teramura, K.; Domen, K. *J. Catal.* **2008**, *254*, 198.
(37) Kato, H.; Hori, M.; Konta, R.; Shimodaira, Y.; Kudo, A. *Chem. Lett.* **2004**, *33*, 1348.
(38) Zou, Z.; Ye, J. H.; Sayama, K.; Arakawa, H. *Nature* **2001**, *414*, 625–627.
(39) Yamashita, H.; Harada, H.; Misaka, J.; Takeuchi, M.; Ikeue, K.; Anpo, M. *J. Photochem. Photobiol., A* **2002**, *148*, 257.
(40) Asahi, R.; Morikawa, T.; Ohwaki, T.; Aoki, K.; Tao, Y. *Science* **2001**, *293*, 269.
(41) Khan, S. U. M.; Al-Shahry, M.; Ingler, W. B., Jr. *Science* **2002**, *297*, 2243.

(42) Hitoki, G.; Takata, T.; Kondo, J.; Hara, M.; Kobayashi, H.; Domen, K. *Chem. Commun.* **2002**, 1698.
(43) Ishikawa, A.; Takata, T.; Kondo, J. N.; Hara, M.; Kobayashi, H.; Domen, K. *J. Am. Chem. Soc.* **2002**, *124*, 13547.
(44) Wang, W. D.; Huang, F. Q.; Liu, C. M.; Lin, X. P.; Shi, J. L. *Mater. Sci. Eng., B* **2007**, *139*, 74.
(45) Pai, M. R.; Singhal, A. M.; Banerjee, A. M.; Tewari, R.; Dey, G. K.; Tyagi, A. K.; Bharadwaj, S. R. *J. Nanosci. Nanotechnol.* **2011** accepted. Pai, M. R.; Banerjee, A. M.; Bharadwaj, S. R.; Kulshreshtha, S. K. *J. Mater. Res.* **2007**, *22*, 1787.
(46) Jakkal, V. S. Powderx: A Fortran software for refining the unit cell parameters from the powder diffraction pattern. Private communication.
(47) Bunn, C. W. *Chemical Crystallograph (translated to Japanese)*; Oxford University Press: Tokyo, Japan, 1961.
(48) Andersen, O. K.; Jepsen, O. *Phys. Rev. Lett.* **1984**, *53*, 2571.
(49) Andersen, O. K.; Jepsen, O.; Glötzel, D. In *Highlights of Condensed Matter Theory*; Bassani, F., Fumi, F., Tosi, M., Eds.; North-Holland: New York, 1985.
(50) Jepsen, O.; Andersen, O. K. *J. Phys.: Condens. Matter* **1995**, *97*, 35.
(51) Lowdin, P. O. *J. Chem. Phys.* **1951**, *19*, 1396.
(52) Paques-Ledent, M. Th. *Spectrochim. Acta, Part A* **1976**, *32*, 1339–1344.
(53) Gaewdang; Chaminade, J. P.; Gravereau, P.; Garcia, A.; Fouassier, C.; Hagenmuller, P.; Mahiou, R. *Mater. Res. Bull.* **1993**, *28*, 1051.
(54) Senthil Kumar, P.; Sunandana, C. S. *Nano Lett.* **2002**, *2*, 975–978.
(55) Sasikala, R.; Sudarsan, V.; Sudakar, C.; Naik, R.; Sakuntala, T.; Bharadwaj, S. R. *Int. J. Hydrogen Energy* **2008**, *33*, 4966–4973.
(56) Qureshi, M.; Chen, H.-Y.; Lu, C.-H. *Solid State Commun.* **2007**, *142*, 85–88.
(57) Hwang, D. W.; Lee, J. S.; Li, W.; Hyuk, Oh. S. *J. Phys. Chem. B* **2003**, *107*, 4963–4970.
(58) Kaneko, M.; Okura, I. *Photocatalysis Science and Technology*; Biological and Medical Physics Series; Kodansha-Springer: Japan, 2002.
(59) Enrico Borgarello, J.; Kiwi, M.; Graetzel, E.; Pelizzetti, M. V. *J. Am. Chem. Soc.* **1982**, *104*, 2996–3002.
(60) Duonghong, D.; Borgarello, E.; Graetzel, M. *J. Am. Chem. Soc.* **1981**, *103*, 4685–4690.
(61) Kato, H.; Kobayashi, H.; Kudo, A. *J. Phys. Chem. B* **2002**, *106*, 12441–12447.